

See discussions, stats, and author profiles for this publication at: <https://www.researchgate.net/publication/224194293>

Development and Preliminary Experimental Validation of a Wind- and Solar-Powered Autonomous Surface Vehicle

Article in IEEE Journal of Oceanic Engineering · November 2010

DOI: 10.1109/JOE.2010.2078311 · Source: IEEE Xplore

CITATIONS

31

2 authors:



Patrick Rynne

University of Miami

14 PUBLICATIONS 295 CITATIONS

SEE PROFILE

READS

7,685



Karl D. von Ellenrieder

Libera Università di Bolzano

105 PUBLICATIONS 1,292 CITATIONS

SEE PROFILE

Development and Preliminary Experimental Validation of a Wind- and Solar-Powered Autonomous Surface Vehicle

Patrick F. Rynne, *Student Member, IEEE*, and Karl D. von Ellenrieder, *Member, IEEE*

Abstract—The design and initial testing of a wind- and solar-powered (WASP) autonomous surface vehicle (ASV) are presented. The concept vehicle is a 4.2-m length overall (L_{OA}) monohull keel-boat powered by a rigid wing sail with a 5-m span. It is designed to operate in 7–10 kn of wind and a maximum sea state of 2. Specific attention is placed on the aerodynamic, hydrodynamic, and systems integration aspects of the design. Rigid wing sails are shown to have superior performance to conventional cloth sails for use on ASVs owing to their higher aerodynamic efficiency and robustness. The manual design process involved in selection of the airfoil cross section for the wing sail and the resulting aerodynamic performance predictions are presented. Through mathematical derivation, the optimal angle for switching the sail configuration from an upwind/crosswind lift-generating mode to a downwind drag-generating mode is found to be 135° . To simplify implementation of the control system when operating in the lift-generating sailing mode, a control scheme that decouples heading and speed control by simply setting the wing sail to an angle of attack of 10° and independently controlling heading was used. The simulation results from a velocity prediction program (VPP) used to verify the feasibility of this control approach are presented. Initial field trials of the vehicle using the control approach with autonomous wing control and manual rudder control are presented. It is shown that the measured boat speeds and wind speed/directions are within the range of values expected from the VPP. Temperatures recorded in a thermal plume during the field trials of the ASV are shown as a function of global positioning system (GPS) location and time.

Index Terms—Autonomous sailboat, autonomous surface vehicle (ASV), ocean observation system.

NOMENCLATURE

A	Planform area.
AR	Aspect ratio.
B	Beam of hull amidships.
C_D	Drag coefficient.

C_{Di}	Induced drag coefficient.
C_L	Lift coefficient.
C_M	Moment coefficient.
C_P	Pressure coefficient.
F_{AR}	Aerodynamic driving force.
F_{AS}	Aerodynamic side force.
F_{net}	Net aerodynamic force.
\overline{GM}	Metacentric height.
\overline{GZ}	Righting arm.
\overline{KG}	Distance keel to center of gravity.
L/D	Lift-to-drag ratio.
L_{OA}	Length overall.
L_{wl}	Length on the waterline.
ORP	Oxidation reduction potential.
P	Pressure.
Re	Reynolds number.
S_w	Wetted surface area.
T	Draft.
U	Freestream velocity.
V_A	Apparent wind velocity.
V_s	Ship velocity.
VPP	Velocity prediction program.
c	Chord length.
m_{hh}	Mass of the bare hull.
t	Airfoil thickness.
u_{10}	Reference velocity 10-m altitude.
∇	Volume displacement.
α	Angle of attack.
β	Apparent wind angle.
ε	Efficiency.
θ	Angle between lift and drag.
ρ	Density.
ϕ	Heel angle.
ψ	True wind direction.

Manuscript received April 29, 2009; revised May 23, 2009 and August 21, 2010; accepted September 12, 2010. Date of publication November 11, 2010; date of current version November 30, 2010. This work was supported by a New Project Development Award from the Florida Atlantic University (FAU) Division of Sponsored Research and the Office of Naval Research under Grant N00014-03-1-0211.

Associate Editor: F. Hover.

The authors are with the Ocean Engineering Department, Florida Atlantic University, Miami, FL 33145 USA (e-mail: patrickrynn@gmail.com).

Color versions of one or more of the figures in this paper are available online at <http://ieeexplore.ieee.org>.

Digital Object Identifier 10.1109/JOE.2010.2078311

I. INTRODUCTION

THE use of unmanned wind-powered autonomous surface vehicles (ASVs) for oceanographic research is an emerging concept of interest in today's environmental and economic climate. As a marine observation tool, it is anticipated that wind-powered ASVs could provide coincident sea surface and air/sea layer data from targeted locations that would feed into research focusing on issues such as: quantifying the strength of air/sea interactions; how local weather and sea surface conditions relate to the mesoscale environment; and how directing *in situ* measurements to specific locations to acquire data in critical regions identified by models (adaptive observations) improves weather forecasting [1]. Despite the extensive history of manned sailboat design, the development of autonomous unmanned versions is still in its infancy. Various configurations including monohulls and catamarans that are propelled by classical cloth sails or rigid wings have emerged throughout the world, yet to date no design has demonstrated the ability to navigate open-ocean conditions over a sustained time period.

The main objective of this pilot study is to identify, explore, and develop the design aspects and technologies required to ultimately make open-ocean-wind-powered ASVs a reality through the development of a concept vehicle. Design issues of particular importance addressed here are: 1) hydrostatic stability and the ASVs self-righting ability; 2) robustness of the sail and airfoil section selection; and 3) navigation and control of a system in which directional and speed control are typically strongly coupled. The concept vehicle is based on a monohull sailboat with an L_{OA} of 4.2 m (13.8 ft), a hull speed (V_s) of about 5 kn and is primarily propelled with a wing sail. This paper begins by addressing some of the aerodynamic and hydrodynamic aspects of the wind- and solar-powered (WASP) vehicle with specific attention placed on combining a specialized wing sail with an existing hull design. A brief overview of the sailing requirements, including identification of the propulsive, reaction, and resistance forces expected is presented to quantify the performance difference between using a rigid wing sail and a classical cloth sail, identify an appropriate airfoil section for a rigid wing, and design the structure of the wing. For the initial field trials of the vehicle, it was sought to simplify the control system by limiting the coupling between speed and heading control. The approach required the wing to set itself at a constant angle of attack with respect to the apparent wind and independently control the rudder to achieve a desired direction. To explore the viability of this approach, a VPP was used to characterize the expected steady-state behavior at all points of sail for a wing angle of attack of 10° to the apparent wind. An overview of the VPP and simulation results is presented. Finally, data are presented from a calm water sea trial used to test the control strategy and serve as a starting point for future work.

II. THE HULL

The hull of the WASP prototype was selected to satisfy time, budget, performance, and adaptability constraints. Among existing sailboat hull designs are three distinct types: dinghies, multihulls, and keelboats. Dinghies are designed with either a

TABLE I
2.4-m HULL PARAMETERS

Parameter	Value
B [m]	0.80
\overline{KG} [m]	0.71
L_{OA} [m]	4.20
Lwl [m]	3.41
m_{bh} [kg]	50.0
T [m]	1.07
S_w [m ²]	4.44
∇ [m ³]	0.38
V_s [knots]	0 – 5

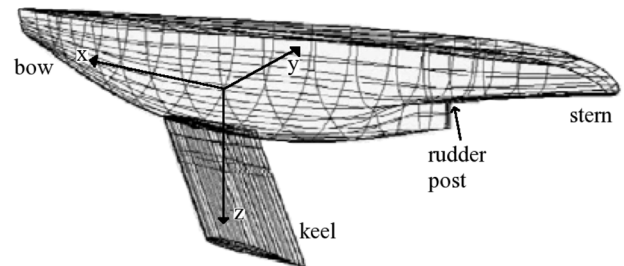


Fig. 1. CAD representation of 2.4-m class sailboat hull (rudder not shown).

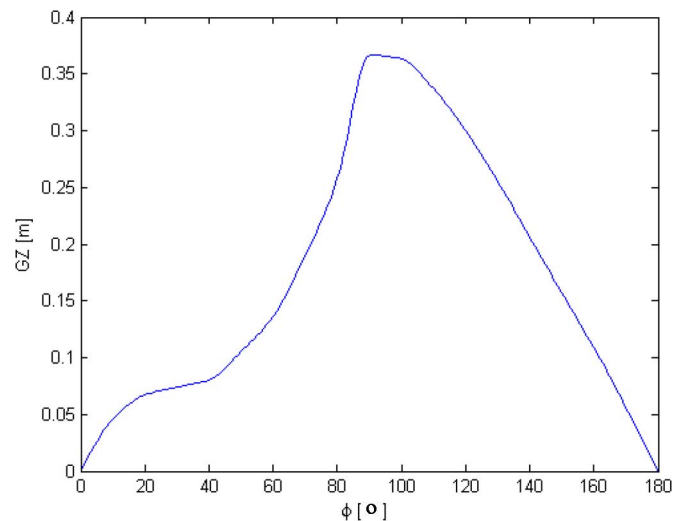


Fig. 2. Analytical righting arm curve: righting arm \overline{GZ} versus heel angle ϕ . The curve was created using a bare hull CAD model in rhino marine.

centerboard or dagger board configuration, and require additional balance to stay upright. As an autonomous vehicle, a weighted keel is needed to ensure stability. Multihulls are inherently stable at low angles of heel, but can capsize and can be almost equally stable upside down. Keelboats are generally the slowest of the three designs, but benefit from upright stability and a self-righting moment across nearly all angles of heel. A keelboat was deemed to be the best choice since it would require the least modification and is a self-righting design. The final selection, a Sodengran 2.4-m class sailboat, is a single-handed displacement vessel requiring no weight shifts (hiking out) for efficient sailing performance. The hull parameters are presented in Table I. The design has been utilized by the sailing community since 1986, and knowledge of its performance is available

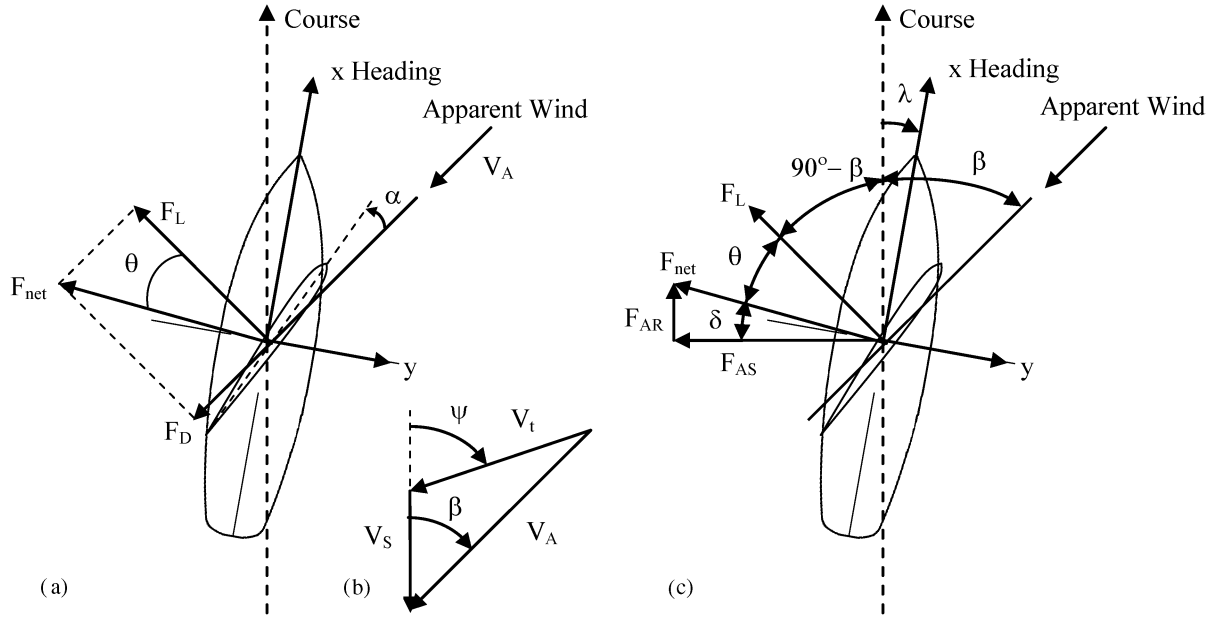


Fig. 3. Sailboat aerodynamic free body diagrams in the boat fixed frame. (a) The airfoil profile represents the wing and α is the angle of attack of the sail with respect to the apparent wind angle. (b) ψ is the true wind direction, β is the apparent wind angle. (c) The x - and y -axes are the boat-fixed maneuvering coordinate system, the x -axis gives the heading while the angle between course and heading is the leeway angle λ . $\delta = (\beta - \theta)$ is the angle between the net aerodynamic force F_{net} and the side force F_{AS} .

through communication with active sailors and designers. Computer-aided design (CAD) hull lines of the Sodengran 2.4-m class sailboat (Fig. 1) were provided by Swedish designer H. Malmsten [2], and are used to determine the righting arm curve (Fig. 2), center of gravity, metacentric height, center of buoyancy, and wetted surface area of the vessel.

The vertical center of gravity of the system was determined by performing a pendulum swing test on the fully loaded/outfitted hull. The WASP was displaced transversely at small angles while suspended from a crane at a fixed height and the period of oscillation was recorded with an inertial measurement unit (IMU). The position of the center of gravity was determined from the measured periods and later corrected for the weight and center of gravity of the wing sail.

III. SAILBOAT AERODYNAMICS

Although the use of composite wings on sailing craft has been pursued, only a few efforts to combine a wing design with an autonomous system have been documented [3]–[5]. Wind-powered propulsion is proven in the sport of sailing in the form of cloth sails. Sails serve the same purpose as wings but generally possess increased drag coefficients caused by appendages such as masts and stanchions [6]. From the perspective of a trained sailor, a cloth sail is easily tuned and controlled. If it is trimmed at too small an angle of attack, the pressure gradient becomes too small to maintain the shape of the cloth and is visible as a “luffing” sail [7]. Luffing a sail in strong winds can be highly destructive and is a major concern in the open ocean. Wings do not luff, but are difficult for a human to control due to a lack of visual input. From the perspective of an automated system, the ability to visualize anything is less important, since feedback can be acquired from nonvisual sensors. Additionally, rigid wings can be controlled on a freestanding rotating mast while sails require

complicated rigging systems. The difference in aerodynamic performance is considered in more detail in Section V.

An angled lifting surface exposed to a fluid in motion creates a pressure gradient that can be expressed as two distinct forces. Lift is generated perpendicular to the incoming free stream velocity while drag acts in the direction parallel to the free stream velocity vector that represents the apparent wind [Fig. 3(a)]. The magnitude of the pressure and forces are defined as

$$P - P_{\infty} = \frac{1}{2} C_P \rho U^2, \quad F_L = \frac{1}{2} C_L \rho U^2 A, \quad F_D = \frac{1}{2} C_D \rho U^2 A. \quad (1)$$

Referring to Fig. 3(a), the lift and drag forces are combined into a single net aerodynamic force whose magnitude and angle relative to the free stream perpendicular are defined as

$$|\vec{F}_{\text{Net}}| = F_{\text{Net}} = \frac{1}{2} \rho U^2 A \sqrt{C_L^2 + C_D^2} \quad (2a)$$

$$\theta = \tan^{-1} \left[\frac{C_D}{C_L} \right]. \quad (2b)$$

As further discussed in Section VI-A, owing to the presence of an atmospheric boundary layer, the apparent wind velocity will generally vary with height above the still water line. Additionally, as the sailboat heels, a spanwise component of the apparent wind develops along the wing sail. The combination of these effects causes the local angle of attack to vary across the span of the wing sail. Thus, the local lift and drag on the wing sail vary as a function of spanwise position and must be integrated to find the total aerodynamic forces and moments. The net aerodynamic force exerted by the wing can be defined with respect to the boat fixed frame. The component parallel to the direction of motion (course) is the aerodynamic driving force (F_{AR}) [8], while that perpendicular to the direction of motion is the aerodynamic side force (F_{AS}). Besides being a function of the angle

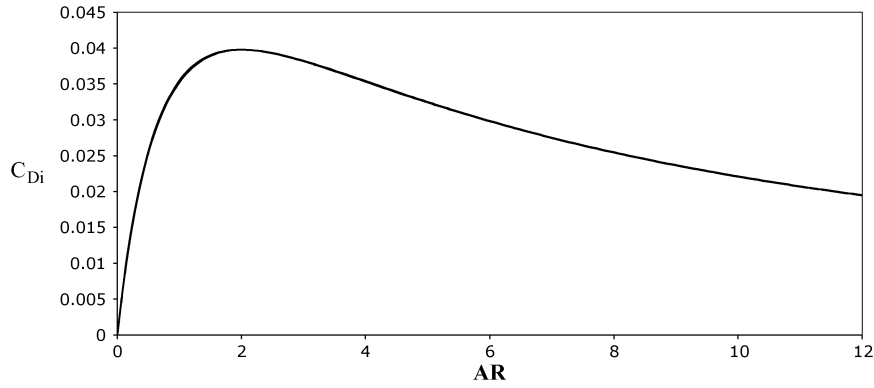


Fig. 4. Approximate effect of AR on C_{Di} of a rectangular symmetric wing using lifting line theory.

of attack of the wing sail (θ is a function of α), F_{AR} and F_{AS} are both dependent on the apparent wind angle and the wind profile in which the vessel is sailing. F_{AR} and F_{AS} are shown in Fig. 3 and defined in

$$F_{AR} = F_{net} \sin(\beta - \theta) \quad (3a)$$

$$F_{AS} = F_{net} \cos(\beta - \theta). \quad (3b)$$

Equation (3) is valid for any lifting surface, whether a rigid wing sail or a cloth sail. For efficient performance of a sailing vehicle, the lifting surface will maximize the aerodynamic driving force while minimizing the aerodynamic side force. At a given leeway angle, the aerodynamic force ratio (F_{AR}/F_{AS}) is at a maximum when θ is minimized. In the limit that $C_D/C_L \rightarrow 0$, the aerodynamic force ratio approaches the limit $F_{AR}/F_{AS} \rightarrow \tan(\beta)$.

IV. AIRFOIL DESIGN

A major step in designing a wing sail is the selection of the 2-D airfoil section. Using the airfoil analysis software XFOIL [9], the performance of a variety of airfoil sections is considered. The WASP section must be symmetrical since the wing sail must generate equal lift on both tacks. A Reynolds number of $Re = 229\,000$ is used as a baseline wind speed value (approximately 7 kn of wind at sea level) as that is the projected operating condition for the testing area and is comparable to past efforts found in published literature [4]. Note that it would have been preferable to design a wing that operates further from the transition range, but the operational Reynolds number for the wing sail was constrained by a combination of manufacturing limitations on the wing chord and the prevailing wind speed at the test site.

Although the section is not quantitatively optimized, particular attention is placed on the evolution of separation and stall at high angles of attack. A characteristic typical of thin airfoils is a relatively strong lift-producing pressure drop at the leading edge with pressure recovery initiating about a quarter to a third of the chord downstream. In comparison, thicker airfoils do not typically have as strong a pressure drop at the leading edge and may not achieve lift coefficients as high as thin foils, but pressure recovery on a thicker foil is generally more gradual. As a result, the lift-producing low-pressure region over a thin airfoil is localized over a smaller region near the leading edge of the airfoil

than it would be on a thick foil of the same chord length. Flow separation may result from the adverse pressure gradient in the pressure recovery region and will typically occur closer to the leading edge on a thin foil than on a thick foil. The magnitude of the lift generated by a thin airfoil will thus be more sensitive to separation as a separation bubble can more easily span a larger proportion of the low-pressure region over the thinner foil and diminish the pressure drop. For this reason, separation over thin foils is more difficult to predict or control. As the WASP wing will be operating at a transitional Reynolds number and may be susceptible to separation, it was decided that use of a thick airfoil section would be preferable.

The XFOIL viscous calculation provides a 2-D analysis of the flow around the wing. For simplicity, the 3-D coefficient of lift is taken as approximately equal to the 2-D model by assuming the wing has sufficiently large aspect ratio [11]. However, the same approximation is not made for the drag coefficient. Two-dimensional analysis does not take into account the induced drag. Induced drag is caused by pressure differences across the wing surface that cause “spillage effects” across the wing tip and result in wing tip vortices. The 3-D coefficient of drag is approximated by adding the 2-D coefficient from XFOIL with an induced drag component (4a) that is calculated using lifting line theory [10], [12] for an angle of attack of 10° [see (4b)]. Note that the 2-D lift coefficient from XFOIL is used to make this calculation (4c) as compared to a more approximate solution for symmetric wings presented in Fig. 4 [12]. This plot illustrates how the induced drag coefficient approaches zero as the wing aspect ratio approaches infinity

$$C_D = C_d + C_{Di} \quad (4a)$$

$$C_{Di} = \frac{C_L^2}{\pi AR} = 0.07 \quad (4b)$$

$$C_D = 0.021 + 0.07 = 0.091. \quad (4c)$$

The manual airfoil design process involved: 1) starting with a baseline airfoil, which is a combination of the National Advisory Committee for Aeronautics (NACA), Joukowski and Van de Vooren sections; 2) creating ten variations of this foil with different leading edge radii (nose thicknesses); 3) for each new radius of curvature creating ten different foils by matching (blending) the nose and the remaining aft section at different chordwise stations; and 4) manually inspecting the lift-to-drag

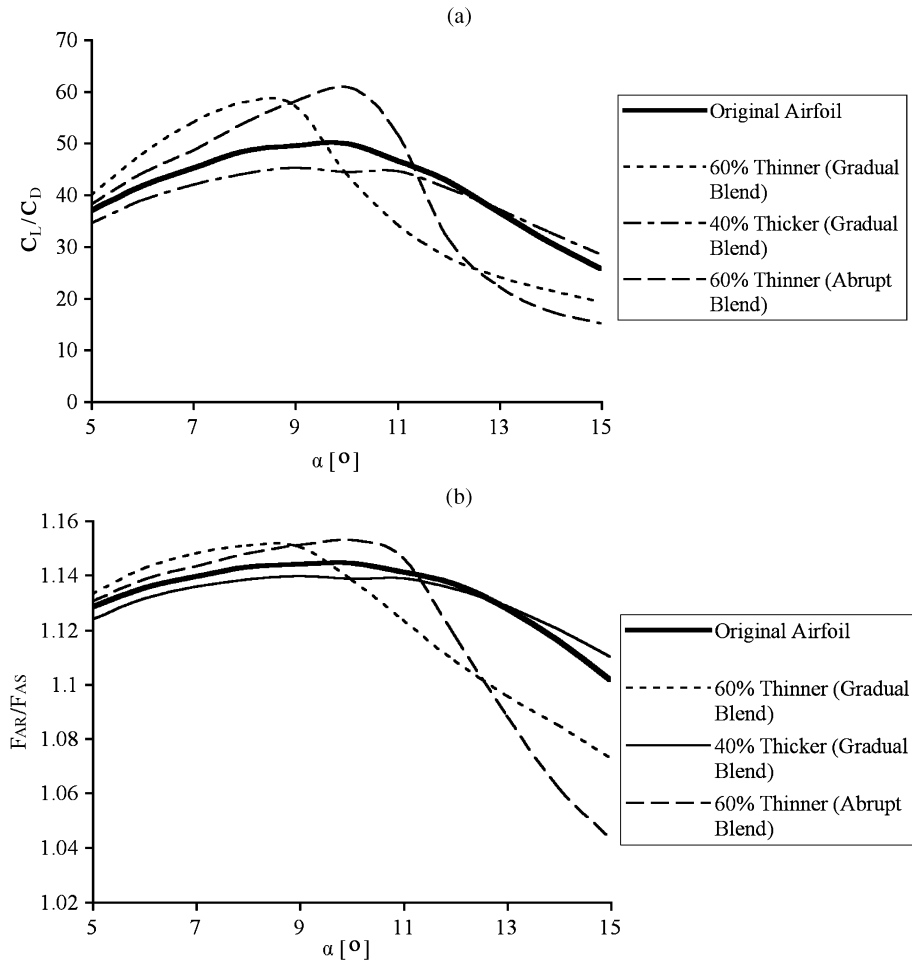


Fig. 5. Effect of leading edge modification on the lift-to-drag ratio and the aerodynamic force ratio in 2-D viscous flow. The position and magnitude of the maximum thickness of each airfoil is the same. $\beta = 50^\circ$ for both figures. Here the airfoil is identified as an “abrupt blend” when the matching occurs fore of the quarter chord point and a gradual blend when the matching location is aft of $x/c = 0.25$.

versus angle-of-attack curves for each foil to identify the one with the highest lift to drag while also exhibiting as little lift dropoff as possible at high angles of attack.

To achieve large lift coefficients, symmetric low Reynolds number airfoils must be very thick (a baseline of 15%–20% is common) [13]. Modifying the nose and streamlining it into the base section shape can affect the pressure distribution, the lift-to-drag ratio, and the general flow characteristics. Two modifications are shown in Fig. 5. A thin nose variation (small leading edge radius of curvature) results from prioritizing a large value of C_L and C_L/C_D . Although the aerodynamic force ratio is high, it is sensitive to angle of attack. For an autonomous system, this is undesirable. When an automated controller negotiates an apparent wind shift caused by sea surface or atmospheric phenomena, the system will not likely be capable of instantly adjusting the angle of attack. The rate of change of angle of attack does not affect the angle at which separation begins [14]. Overall, it is expected that the wing sail will operate within a range of angles of attack, making narrow nose variations a poor choice. Fig. 5 suggests that increasing the nose thickness improves the larger angle-of-attack performance, but decreases the smaller angle-of-attack performance. The trend shows that a thicker nose section makes the aerodynamic force ratio “flatten” out. A flat aerodynamic force ratio

response over the angle of attacks of interest is attractive as a conservative design choice.

The airfoil selected for the wing has a maximum thickness of $t/c = 0.2$ at the chordwise position $x/c = 0.25$ and corresponds to the “40% thicker (gradual blend)” section in Fig. 5. Fig. 6 shows that the minimum pressure occurs within the first 10% of the chord. The pressure immediately begins its recovery along the entire section. Separation is a concern with any low Reynolds number airfoil, and will likely occur in the unsteady free stream of an open-ocean environment. Instead of designing to prevent separation and stall, the WASP section is designed to maintain $F_{AR}/F_{AS} > 1$, for $0^\circ < \alpha \leq 15^\circ$. XFOIL is used to analyze the streamlines of the foil in 2-D viscous flow to check for visibly separated regions including separation bubbles. XFOIL analyses do not suggest that separation will occur until an approximate angle of attack of 15° . For this foil, flow separation initiates off the trailing edge with no separation bubbles present on the leading edge. Analysis of the aerodynamic force ratio for the above section along with two modified sections for $5^\circ \leq \alpha \leq 15^\circ$ is shown in Fig. 5(b).

V. SAIL VERSUS WING SAIL

Although the aerodynamic performance of cloth sails is satisfactory for sailing craft [6], a wing sail is selected as the best

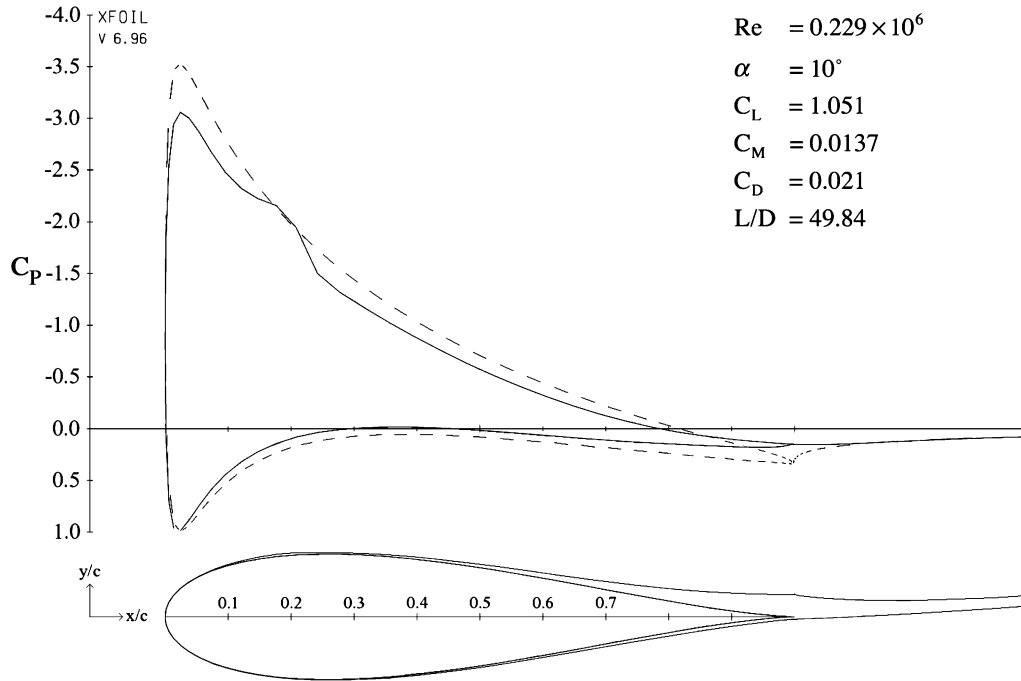


Fig. 6. XFOIL 2-D viscous pressure distribution. The pressure coefficient $(p - p_\infty)/0.5\rho U^2$, where p is the local pressure and p_∞ is the freestream pressure, is plotted as a function of chordwise position x/c . Note that the vertical axis is inverted. The dashed line is the inviscid solution and the solid line is the viscous solution. The boundary layer thickness and rotational wake are portrayed about the airfoil section outline in the lower part of the figure.

TABLE II
CLOTH SAIL VERSUS RIGID WING SAIL

	Cloth Sail	Rigid Wingsail
C_L	1.056	0.910
C_D	0.359	0.151
β	50.0°	50.0°
ϵ	50.9%	71.8%

candidate for the proposed control system. An additional benefit of using the wing sail is its higher aerodynamic efficiency ϵ , defined as

$$\frac{F_{AR}}{F_{AS}} = \tan(\beta - \theta) \quad (5a)$$

$$\lim_{C_L, \lambda \rightarrow 0} \frac{F_{AR}}{F_{AS}} = \tan \beta \quad (5b)$$

$$\epsilon \equiv \frac{F_{AR}}{F_{AS}} = \frac{\tan(\beta - \theta)}{\tan \beta} \quad (5c)$$

In Table II, the aerodynamic efficiency of the existing 2.4-m class sail and the WASP rigid wing sail are compared. Here, a Reynolds number of $Re = 229\,000$ (corresponding to an apparent wind strength of 7 kn), an apparent wind angle of $\beta = 50^\circ$ (upwind sailing) and an angle of attack of $\alpha = 10^\circ$ are used. The lift and drag coefficients of the cloth sail are determined using Hazen's model [12].

From (5) and (2b), it can be seen that both coefficients of lift and drag are important for maximizing the efficiency of a

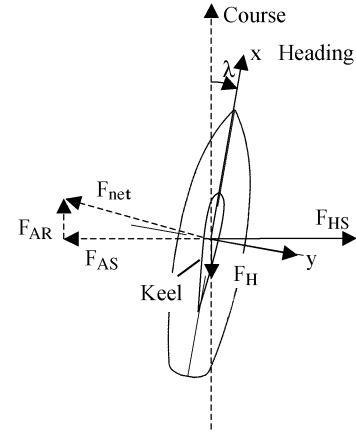


Fig. 7. Sailboat hydrodynamic free body diagram in the boat fixed frame. The hydrofoil profile represents the keel. At equilibrium, the hydrodynamic side force F_{HS} balances the aerodynamic side force F_{AS} and the force of hydrodynamic resistance F_{HR} balances the aerodynamic driving force F_{AR} , where F_{HS} and F_{HR} are perpendicular and parallel, respectively, to the course direction. Note that F_{HS} is generated by the keel and hull acting as an underwater wing with the leeway angle λ being the angle of attack.

lifting surface. It is a common misinterpretation that wings provide more lift than cloth sails. In fact, the lift coefficients of symmetric wings and modern cambered cloth sails are typically similar [6]. However, wings benefit from smaller drag coefficients, and their higher efficiency is a result of that characteristic.

Wing sail or cloth sail selection also affects the equilibrium leeway angle λ . λ can be thought of as the minimum angle of attack of the submersed keel and rudder required to counteract the aerodynamic side force (Fig. 7). If the cloth sail or wing sail system were to create excessive drag, the aerodynamic force ratio could become small enough to effectively stall the keel

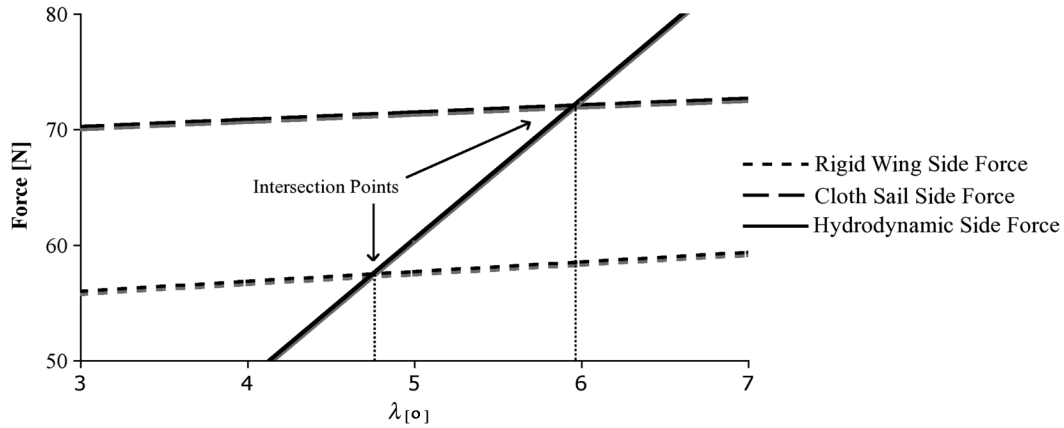


Fig. 8. Leeway angle approximation: apparent wind speed is $|\vec{V}_A| = 7$ kn, $\beta = 50^\circ$.

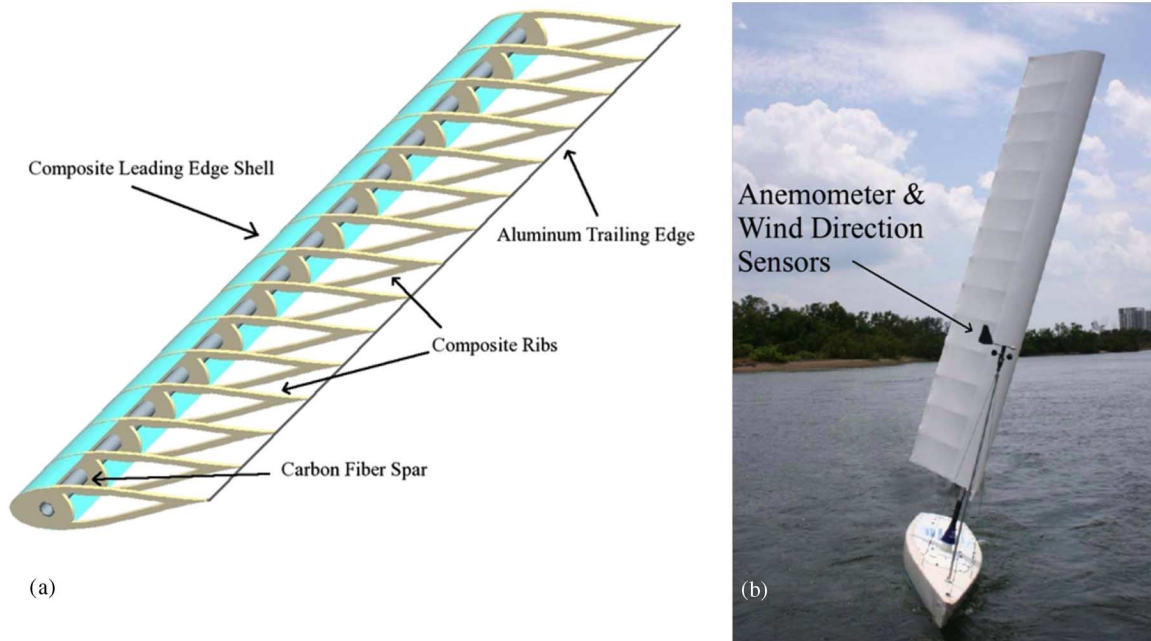


Fig. 9. (a) Final WASP wing sail assembly consists of a carbon fiber spar, epoxy/fiberglass reinforced syntactic foam ribs, composite leading edge shell, aluminum trailing edge, and ultraviolet light resistant marine polymer. The total mass is 18 kg. (b) The WASP during a field trial.

and rudder. In this case, the vehicle would slide sideways in the downwind direction [7], known in sailing terminology as “side slipping.” Here, the keel and rudder are modeled as low aspect ratio symmetric wings using the same governing equations presented for the rigid wing sail [12]. As shown in Fig. 8, the theoretical leeway angle solutions suggest that a cloth sail system would exhibit a slightly larger leeway angle, and hence a higher induced drag, than a wing sail system.

Here we have compared a wing sail of rectangular planform, rather than tapered, and the triangular cloth sails conventionally found on 2.4-m class sailboats. Note that the center of pressure of triangular or tapered sails is located closer to the water surface where the wind speed is lower, which generates a lower heeling moment than would be found on a sail of rectangular planform of the same propulsive power. However, at the same time, a sail of rectangular planform has less induced drag than a triangular cloth sail because it has less spillage near the top of the sail. In addition, while fabrication and construction of trian-

gular or tapered cloth sails is relatively simple, the construction of a tapered or triangular wing sails is more complex and expensive than a wing sail of rectangular planform.

Based on the above aerodynamic, hydrodynamic, fabrication, and control considerations, a wing sail [Fig. 9(a)] is chosen. A single element wing sail is selected over a potentially more aerodynamically efficient multielement wing sail to simplify the fabrication process and wing trimming system. Using this approach, a single stepper motor can be used within the hull to trim the wing as shown in Figs. 9(b) and 13. It is anticipated that future efforts would benefit from a multielement approach provided that the weight, cost, reliability, and fabrication penalties associated with the added mechanical complexity do not outweigh the benefits of improved aerodynamic performance.

VI. VELOCITY PREDICTION PROGRAM

Unlike motorized vessels, sailboats require the use of tacking and jibing maneuvers to reach a desired location and the max-

imum attainable speed is dependent on point of sail (heading). Thus, a combination of route planning for navigation [15] and lower level control systems for maneuvering [16] is generally required for a fully autonomous sailboat to reach a specified target zone. Route planning algorithms require obstacle avoidance detection inputs as well as environmental inputs like wind, current, and sea state data to determine an optimal course. Obstacle avoidance could involve development of predefined lookup maps for static obstacles and the use of a combination of techniques, such as thermal imaging, radar, camera, and automatic identification systems for the detection of dynamic obstacles [17]. For sustained oceanographic/meteorological measurement applications, additional route planning inputs would likely include weather and sea state forecasting, adaptive sampling, multivehicle cooperation, and remote supervisory control. The lower level maneuvering control systems would involve actuating the rudder to provide corrections between the actual heading and the desired heading and modulating the sail for speed control.

In general, the heading and speed of a sailboat are strongly coupled. For the initial field trials of the vehicle, it was desired to simplify the control system by decoupling the control of speed and heading. The approach adopted was to minimally control speed, by always commanding the wing to set itself at a constant angle of attack with respect to the apparent wind, as measured by the onboard wind direction sensor, and manually control the rudder to achieve a desired direction. A main additional benefit of this approach is that it permits safer supervisory control of the vehicle during the field trials, which were conducted in a relatively busy section of the U.S. Intracoastal Waterway located near Port Everglades, FL. To explore the feasibility of this approach, a VPP was used to characterize the expected steady-state behavior at all points of sail for a wing angle of attack of 10° to the apparent wind. The VPP was used to compute boat speed, heel angle, leeway angle, and apparent wind direction as a function of wind direction.

A VPP calculates the orientation and speed of a sailing vessel when it is in steady-state force and moment equilibrium. Rather than solving the equilibrium conditions for all six degrees of freedom, it is common, as is done here, to only compute force equilibrium in the transverse and longitudinal directions and for moment equilibrium about the longitudinal axis [12]. The flow of wind over the sail generates aerodynamic lift (which is perpendicular to the local apparent wind direction at the wing) and drag (which is parallel to the local apparent wind). In the boat-fixed frame of reference, the resultant aerodynamic force has components in both the longitudinal and transverse directions. Owing to the aerodynamic lever arm, which extends from the center of aerodynamic pressure on the wing sail to the center of flotation at the waterplane, the aerodynamically generated transverse force also produces a heeling moment about the longitudinal axis. The aerodynamically generated forces [Fig. 3(a) and (b)] are balanced by the hydrodynamically generated forces (Fig. 7) on the hull: 1) aerodynamic thrust is balanced by hull resistance; and 2) the hull moves at a small leeway angle with respect to the boat's trajectory, which gives rise to a keel-generated lift force that lies perpendicularly to the boat's trajectory and balances the transverse aerodynamic

force. The aerodynamically generated moment is balanced by a hydrostatic righting couple, which arises from the transverse misalignment between the center of buoyancy of the submerged hull and the overall center of gravity of the vessel. The iterative procedure outlined in [12] was used to solve the equilibrium conditions as a function of wind speed and direction; the specific models employed in the computations include the following.

A. Aerodynamic Forces

The calculation of lift and drag, and the resultant thrust and side forces, produced by the wing sail first requires the determination of the local velocity vector at points along the span of the wing. The apparent wind experienced at the boat differs from the true wind and will be the vector sum of boat velocity and wind velocity. Owing to the atmospheric boundary layer at the water's surface, the wind speed will vary with height, causing a gradient between the base and the top of the sail, which must be taken into account. In addition, as the boat heels and the wing is given different angles of attack, the orientation of the apparent wind changes with respect to a wing-fixed coordinate system.

To include each of these effects in the VPP simulation, the local apparent wind velocity vector was first computed at several spanwise stations along the wing for each boat speed, wind speed, and wind direction. Employing conventional 3-D maneuvering coordinate systems for the boat and wing, Euler angle coordinate transformations were applied to the apparent wind velocity vector transforming it from a boat-fixed frame into wing-fixed coordinate system and then finally into a coordinate system defined by the local freestream velocity vector in the plane of each of the airfoil sections making up the wing. In this plane, the local lift and drag are calculated and then transformed back to a boat-fixed coordinate system. Once the forward and side forces are calculated at each spanwise station along the wing, they are used to find the total side force, total thrust, and the aerodynamic moment arm.

The experimental phase of testing was conducted in the fetch-limited U.S. Intracoastal Waterway. In the absence of a measured wind velocity profile and measured fetch data for the field tests, the wind gradient existing between the base and the top of the sail was accounted for in the VPP by using the open-ocean wind model

$$\frac{u}{u_{10}} = \left(\frac{z}{10}\right)^{1/7} \quad (6)$$

where z is the height in meters above the still water line and u_{10} is the 1 h averaged wind speed at 10-m altitude [18].

The aerodynamics of a wing sail trimmed at a small angle of attack is substantially different from a classical cloth sail at large apparent wind angles. In a classical sailboat, the cloth sail performs like a lifting surface for apparent wind angles less than $\beta \approx 90^\circ$. However, for greater angles, the sail is trimmed such that it behaves like a parachute, or blunt body. A clear example of this are the brightly colored downwind sails called spinnakers that effectively "catch" the wind. Fig. 10(a) and (b) illustrates the difference between using a wing sail as a lifting surface and as a blunt body for large apparent wind angles. As a blunt body, the only force created is drag. The point on the apparent wind

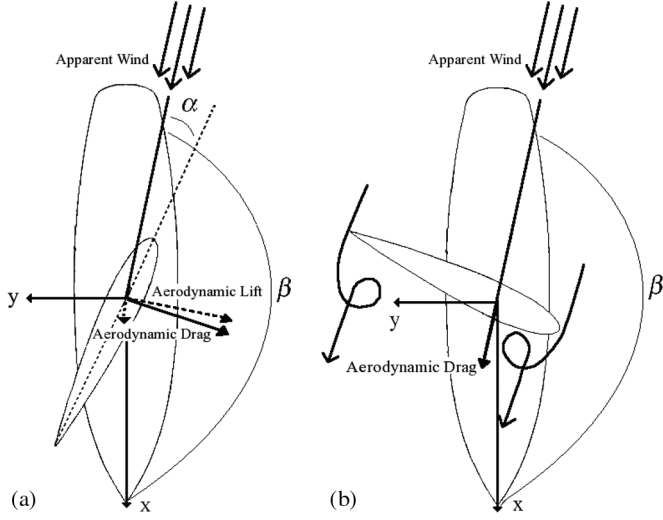


Fig. 10. For downwind sailing, the wing sail can be trimmed (a) as a lifting surface at a small angle of attack or (b) as a blunt body at a large angle of attack.

curve where it becomes beneficial to switch modes can be found by equating the aerodynamic driving force F_{AR} [see (3a)] obtained by each mode

$$\begin{aligned}
 C_{L(\text{blunt})} &= 0 \\
 C_{D(\text{blunt})} &\approx 1.2 \\
 \sin \left[\beta - \tan^{-1} \left(\frac{C_{D(\text{wing})}}{C_{L(\text{wing})}} \right) \right] \\
 &\times \frac{1}{2} \rho U^2 A \sqrt{C_{L(\text{wing})}^2 + C_{D(\text{wing})}^2} \\
 &= \sin \left[\beta - \tan^{-1} \left(\frac{C_{D(\text{blunt})}}{C_{L(\text{blunt})}} \right) \right] \frac{1}{2} \rho U^2 A C_{D(\text{blunt})}. \quad (7)
 \end{aligned}$$

The lift and drag coefficients of the selected airfoil (Section III) are given by the following polynomial fits for $5^\circ \leq \alpha \leq 15^\circ$:

$$\begin{aligned}
 C_L &= -0.0002\alpha^3 + 0.0018\alpha^2 + 0.114\alpha \\
 C_D &= -0.00002\alpha^3 + 0.0009\alpha^2 + 0.0015\alpha + 0.00991. \quad (8)
 \end{aligned}$$

where α is in degrees. For an angle of attack of $\alpha = 10^\circ$ and apparent wind angles of $\beta \geq 135^\circ$, it is more beneficial to switch between the modes and trim the wing sail at a right angle to the wind so that it acts as parachute (zero net circulation, fully separated flow) rather than a lifting surface.

B. Hydrodynamic Resistance Models

The total hydrodynamic resistance was calculated as the sum of the frictional resistance R_F , residuary resistance (wave-making and pressure drag) R_R , and heeling resistance R_H . It is assumed that the sailboat is making way in calm, flat water so that the added resistance of moving through waves is neglected. Hull surface roughness resistance was also neglected because, at the low L_{wl} -based Reynolds numbers expected, the hull is hydraulically smooth [18].

The frictional resistance was calculated from the 1957 International Towing Tank Conference (ITTC) Line and the resid-

uary resistance was determined using the regression models developed from the Delft Systematic Yacht Hull (DSYH) Series [12], [19]. For both the R_F and R_R calculations, as is conventional, it was assumed that the upright hull form characteristics could be used in the regression models. The heeling resistance R_H was also calculated using a regression model from the DSYH Series [18], [19].

C. Hydrodynamic Keel Model

The keel utilizes a 15%-thick section with the maximum thickness located about 38% of the chord aft of the leading edge. As a NACA 63₂ - 015 airfoil section has similar characteristics, the lift and drag coefficients for this section were used in the hydrodynamic model of the keel.

D. Hydrostatic Righting Moment Model

The product of the righting arm curve computed in Fig. 2 and the total weight of the sailboat was utilized in the VPP to determine the righting moment at each heel angle.

E. Assumptions/Conditions applied in the VPP

- 1) Three-dimensional effects on the drag of the wing are calculated using lifting line theory. The existence of wing tip vortices effectively increases the drag coefficient and reduces the lift coefficient [12].
- 2) The regression models developed for the DSYH Series are also applicable to the 2.4-m sailboat hull. Empirically determining all of the resistance components of the 2.4-m sailboat was not feasible given time and financial constraints.
- 3) The wetted surface area is constant. The wetted surface area and frictional component of hull resistance will change with different heel angles. Future empirical tests are needed to quantify this change.
- 4) The righting moment is calculated using the CAD-generated righting arm curve presented in Fig. 2.
- 5) The heel angle will be $|\phi| \leq 45^\circ$, which is the maximum suggested heel angle from designers and racers of 2.4-m class sailboat.
- 6) The magnitude and direction of the wind is constant.
- 7) For apparent wind angles of $\beta \leq 135^\circ$, the angle of attack will be $\alpha = 10^\circ$.
- 8) For apparent wind angles of $\beta > 135^\circ$, the angle of attack will be $\alpha = 90^\circ$ (Fig. 10).

F. VPP Results

The results of the VPP are shown in Fig. 11. V_S is maximized at apparent wind angles of $\beta = 90^\circ$. As the apparent wind angle decreases from $\beta = 90^\circ$, the induced heel caused by the aerodynamic side force increases.

VII. SYSTEM HARDWARE

One of the primary challenges in the development of the WASP vehicle is system integration [20]. Three principle subsystems are presented: navigation and control, propulsion, and data acquisition. The primary sensors of the navigation

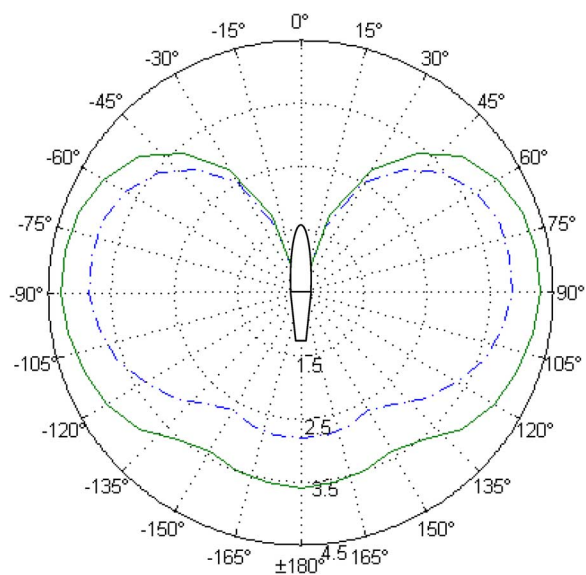


Fig. 11. Velocity prediction plot for $u_{10} = 10.0$ kn “- - -” and $u_{10} = 12.6$ kn “—” of true wind. True wind direction corresponds to the angle from the vertical direction, and the resulting boat speed in knots appears as a radial distance from the origin. The speed is maximized at apparent wind angles of $\beta = 90^\circ$ (beam reaching).

TABLE III
CONTROL SYSTEM HARDWARE

Sensor	Model
Processor	LPC 2138 Microcontroller
GPS	FV-M8 32 Channel 5Hz Receiver
Digital Compass	OS5000-S Tilt Compensated Compass
Anemometer	NovaLynx 200-WS-02

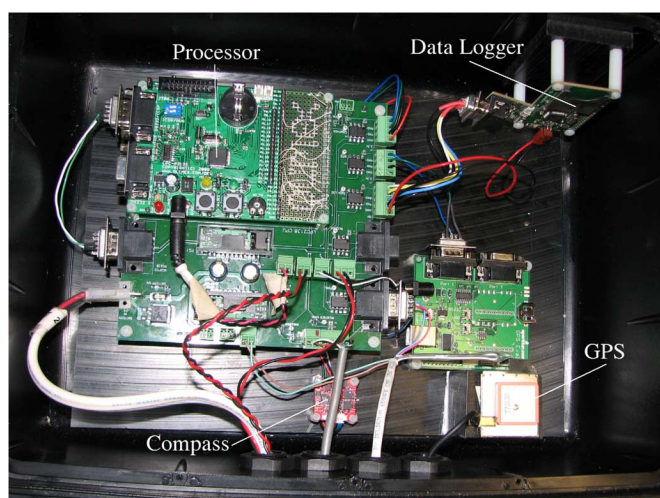


Fig. 12. Core components of the navigation and control systems.

and control system are presented in Table III. The continued evolution of this category of small, low-power electronics nurtures the development of energy-harvesting autonomous marine vehicles such as the WASP [21].

The final control assembly is mounted within a $20 \times 15 \times 10$ cm³ waterproof case as shown in Fig. 12. The system is designed to be transferable to other vehicles. For example, in

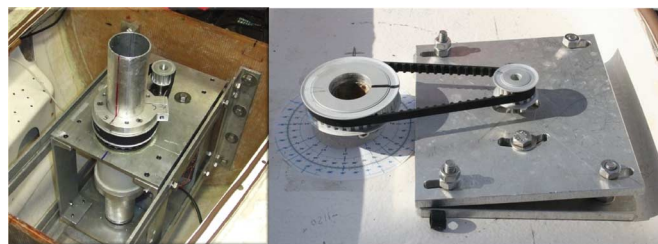


Fig. 13. Wing sail and rudder are controlled with high-torque stepper motors mounted beneath the deck.



Fig. 14. CAD representation and photo of the thru-hull sensor suite. From left to right are the ORP, pH, dissolved oxygen, and salinity probes.

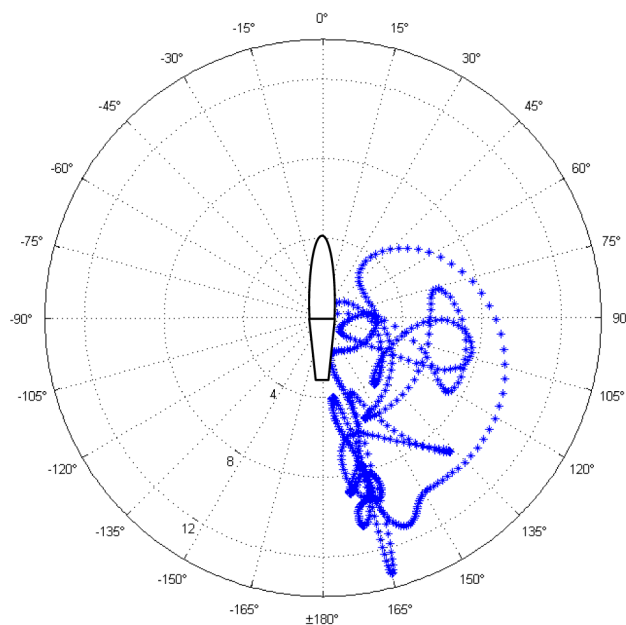


Fig. 15. True wind direction versus true wind speed (polar radius in knots) as determined from data collected onboard the WASP during initial field trials. It is assumed that the water is stationary (no currents).

2009, the same unit was used to control a visual-based navigation system of a conventionally propelled (propeller driven) ASV [22].

The WASP is primarily propelled by the force generated by the wing sail and steered by the actuation of the rudder. Both the wing sail and rudder are physically manipulated with high-torque stepper motors that communicate through RS232 connections with the navigation and control system. Position feedback is achieved with rotary encoders. The stepper motor assembly for both the wing sail and rudder is shown in Fig. 13.

As a proof of concept, a water quality sensor suite and data acquisition system are included. Air temperature, water temper-

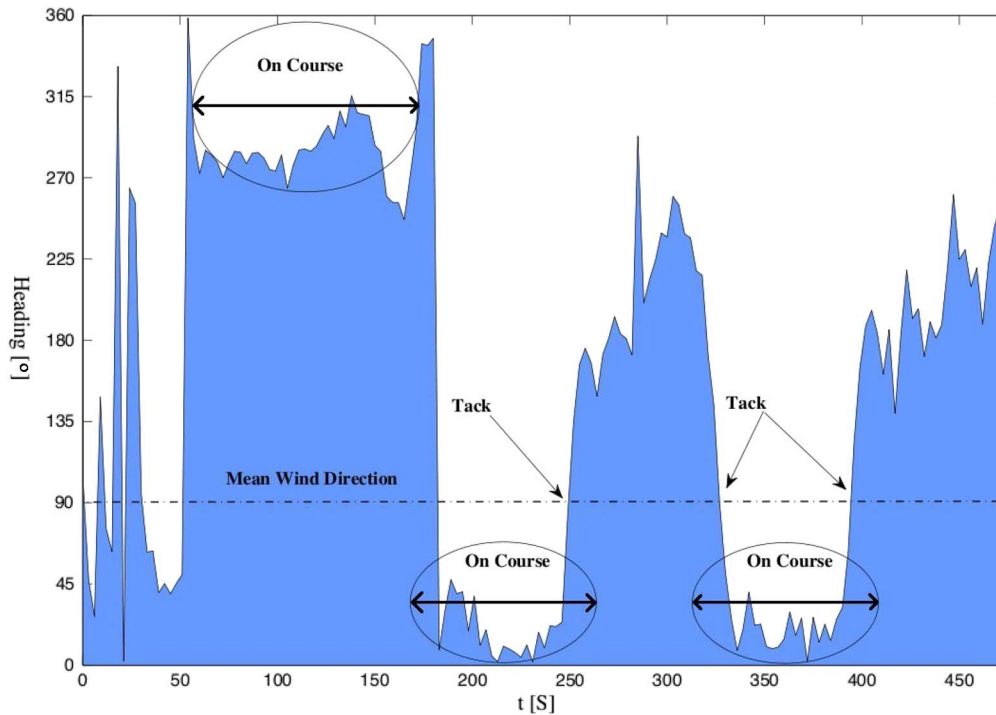


Fig. 16. Heading time series. The heading is referenced with respect to the local North using a magnetic flux gate compass.

ature, salinity, ORP, pH, and dissolved oxygen sensors are used to record sea surface parameters. The sensors are mounted beneath the waterline at the transom to prevent disturbance of the flow upstream of either the keel or rudder (Fig. 14).

VIII. INITIAL RESULTS

A. A Comparison of Measured and Predicted Performance

The first experiment was conducted in a closed water environment in a south/southeasterly wind; the true wind speed varied between about 0.5 and 13 kn, with an average speed of 5 kn (Fig. 15). There were no waves in the testing area and the tide was slack (no visible current). The experiment lasted about 7.5 min.

During this test, the angle of attack of the wing sail was controlled autonomously while rudder angle instructions were transmitted wirelessly from a shore-based computer to the on-board system. The heading of the WASP during the experiment is presented in Fig. 16.

The highlighted regions illustrate a straight course and turning maneuver. Although minimum rudder changes were made during the straight segments of the test, the change in wind strength and direction affected the heel angle significantly. Varying heel angles induce yawing moments [12] and account for the oscillations in the heading.

Taking advantage of the minimal presence of surface waves and current during the experiment, these data were used to analyze the validity of the velocity prediction model. The results are presented in Fig. 17 in the form of recorded data points plotted on a VPP polar plot. Some data processing was implemented in this figure; specifically the data correlating with a tacking maneuver (turning the bow through the wind) were removed. These points suggest high speeds at low apparent wind

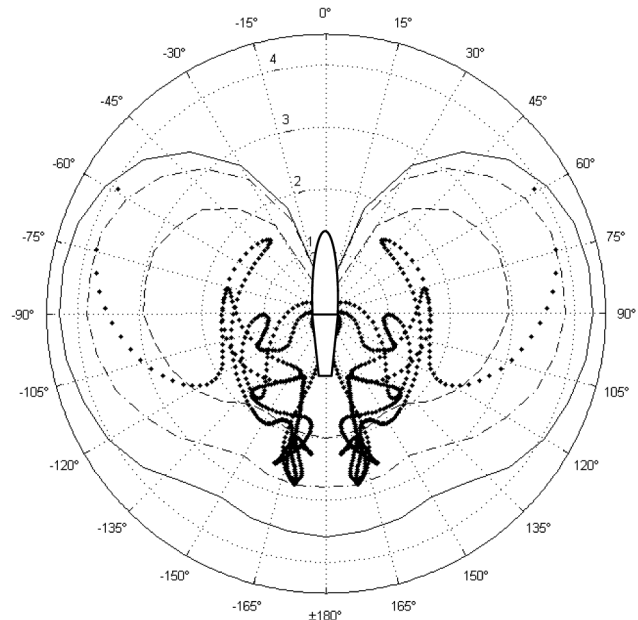


Fig. 17. Sea trial velocity distribution and numerical velocity prediction. Speed over ground (SOG) in knots versus boatspeed polar for $u_{10} = 7.55$ kn “—” (6 kn at 2-m altitude), 10.0 kn “- - -”, and $u_{10} = 12.6$ kn (10 kn at 2-m altitude) “.” of true wind.

angles, but were found to be a result of momentum effects rather than steady-state equilibrium. While following a straight course, the WASP will accelerate until it reaches steady state. With enough momentum, a 180° turning maneuver through the wind (tacking) can be accomplished. If a tacking maneuver were initiated while the vehicle was at rest, it would likely fail to turn through the wind due to a diminishing aerodynamic driving

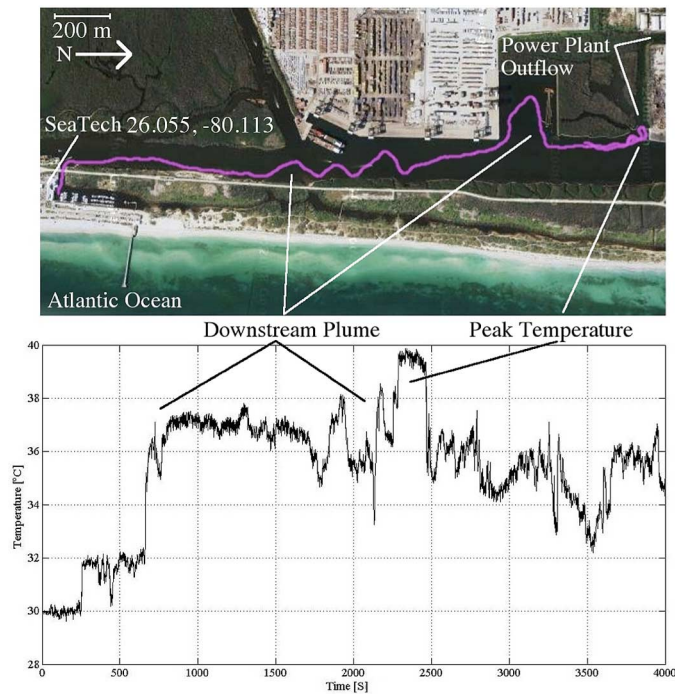


Fig. 18. GPS plot and sea surface temperature data collected by the WASP during a mission in the Fort Lauderdale Intracoastal Waterway. Note the elevated downstream temperatures caused by the outflow from a local power plant cooling station.

force as defined in (3). The mean wind speed during the experiment was $|\vec{V}| = 5$ kn. Nearly all of the data points fall within the steady-state envelope given by the dashed curve for $u_{10} = 7.55$ kn, meaning that the equilibrium velocity predicted by the simulation is generally higher than the observed performance of the WASP.

This is not surprising since the VPP predicts the maximum velocity as a function of true wind angle, not the instantaneous velocity for any given condition. To robustly test the accuracy of the VPP, a sufficiently large testing area with steady wind strength is needed to allow the vehicle to reach steady state for each particular point of sail. The results presented here represent quasi steady state, since the vehicle did not have ample space to reach equilibrium and the wind strength and direction varied.

B. Water Quality Sampling Measurements

A second experiment was conducted in the U.S. Intracoastal Waterway in Port Everglades, FL, during a flooding tide. The purpose of this experiment was to direct the WASP into an oceanographic area of interest to collect sea surface data as a proof of concept. The target, a thermal plume caused by the outflow from a local power plant is located 2.2 km North of the Florida Atlantic University SeaTech Campus. Sea surface temperature data and the vehicle's GPS track are shown in Fig. 18. The wind speed during this experiment ranged from 5 to 15 kn and was highly oscillatory due to upwind obstacles (trees, buildings, etc.). No performance data from this experiment are presented due to the nonuniform effects of the strong current present in the waterway. To illustrate, near the beginning of the

mission the current was very low, and the WASP was able to make slow northerly headway towards the plume. As the vehicle approached the outflow channel of the power plant, the current increased and the wind died, making northerly headway impossible. Eventually the vehicle began drifting to the south and the mission was aborted. Further discussion of this experiment can be found in [1].

IX. CONCLUDING REMARKS

Design considerations in the development of a WASP ASV have been presented. The combination of a rigid wing sail of high aerodynamic efficiency paired with a self-righting monohull craft is suitable for an ASV designed to operate in flat-water conditions and should also be considered for open-ocean designs. A long-term goal of this research is to develop a fully autonomous long-range surface vehicle for general oceanographic and meteorological observations at the air/sea boundary. Future work towards this goal includes implementation of a fully autonomous control system (both rudder and sail), energy harvesting, and power management subsystems along with increasing the physical robustness of the vehicle. Additionally, expanding the operating wind speed and sea state capabilities towards true open-ocean conditions, including the survivability in extreme conditions, will be critical milestones in this effort.

ACKNOWLEDGMENT

The authors would like to thank M. Tall and Prof. N. Xiros for substantial contributions to the command and control system, S. Clark for insight regarding the design and fabrication of sailboat wing sails, and T. Furfaro for many hours of general engineering expertise. This vehicle was developed in collaboration with the 2007–2008 Florida Atlantic University (FAU) Department of Ocean Engineering Senior Design WASP ASV Team.

REFERENCES

- [1] P. F. Rynne and K. D. von Ellenrieder, "Unmanned autonomous sailing: Current status and future role in sustained ocean observations," *Mar. Technol. Soc. J.*, vol. 43, no. 1, pp. 21–30, 2009.
- [2] H. Malmsten, *Private Communication*. 2008, Malmsten Boats Inc., Goteborg, Sweden.
- [3] E. W. Schlieben, "SKAMP—An amazing unmanned sailboat!," *Ocean Ind.*, pp. 38–43, Sep. 1969.
- [4] G. H. Elkaim, "System identification for precision control of a wing-sailed GPS-guided catamaran," Ph.D. dissertation, Dept. Aeronaut. Astronaut., Stanford Univ., Stanford, CA, 2002.
- [5] C. M. Sauze and M. Neal, "Design considerations for sailing robots performing long term autonomous oceanography," in *Proc. Int. Robot. Sailing Conf.*, Breitenbrunn, Austria, 2008, pp. 21–29.
- [6] W. S. Bradfield and S. Madhavan, "Wing sail versus soft rig: An analysis of the Successful Little America's Cup Challenge of 1976," in *Proc. 3rd Chesapeake Sailing Yacht Symp.*, Annapolis, MD, Jan. 15, 1977, pp. 97–110.
- [7] F. Bethwaite, *High Performance Sailing*. Camden, ME: International Marine, 1993, pp. 188–194.
- [8] J. H. Milgram, "Fluid mechanics for sailing vessel design," *Annu. Rev. Fluid Mech.*, pp. 613–616, 1998.
- [9] M. Drela, "XFOIL: An analysis and design system for low Reynolds number airfoils," in *Low Reynolds Number Aerodynamics*, ser. Lecture Notes in Engineering, T. J. Mueller, Ed. New York: Springer-Verlag, 1989, vol. 54, pp. 1–12.
- [10] J. D. Anderson, *Fundamentals of Aerodynamics*. Blacklick, OH: McGraw-Hill, 1984, pp. 490–491.

- [11] M. Drela, "MIT course 16.810 lecture notes—XFOIL and low speed airfoil design/analysis," unpublished.
- [12] L. Larson and R. Eliasson, *Principles of Yacht Design*. Blacklick, OH: McGraw-Hill, 2000, pp. 56–95.
- [13] G. H. Elkaim, "Airfoil section design and configuration analysis of a free-rotating wing-sail for an autonomous marine surface vehicle," *AIAA J. Aircraft*, submitted for publication.
- [14] M. M. Koochesfahani and V. Smiljanovski, "Initial acceleration effects on flow evolution around airfoils pitching to high angles of attack," *AIAA J.*, vol. 31, no. 8, pp. 1529–1531, 1993.
- [15] R. Stelzer and T. Pröll, "Autonomous sailboat navigation for short course racing," *J. Robot. Autonom. Syst.*, vol. 56, no. 7, pp. 604–614, 2008.
- [16] R. Stelzer, T. Pröll, and R. I. John, "Fuzzy logic control system for autonomous sailboats," in *Proc. IEEE Int. Conf. Fuzzy Syst.*, London, U.K., 2007, pp. 97–102.
- [17] R. Stelzer, K. Jafarmadar, H. Hassler, and R. Charwot, "A reactive approach to obstacle avoidance in autonomous sailing," in *Proc. Int. Robot. Sailing Conf.*, Kingston, ON, Canada, 2010, pp. 34–40.
- [18] O. M. Faltinsen, *Hydrodynamics of High-Speed Marine Vehicles*. New York: Cambridge Univ. Press, 2005, pp. 28–39.
- [19] J. A. Keuning and U. B. Sonnenberg, "Approximation of the hydrodynamic forces on a sailing yacht based on the delft systematic yacht hull series," in *Proc. Int. HISWA Symp. Yacht Design Yacht Construction*, 1998, pp. 101–137.
- [20] P. F. Rynne, "Design and performance of a wind & solar-powered autonomous surface vehicle," M.S. thesis, Dept. Ocean Eng., Florida Atlantic Univ., Boca Raton, FL, 2008.
- [21] N. A. Cruz, "Autonomous sailboats: An emerging technology for ocean sampling and surveillance," in *Proc. MTS/IEEE OCEANS Conf.*, Quebec City, QC, Canada, 2008, DOI: 10.1109/OCEANS.2008.5152113.
- [22] M. H. Tall, P. F. Rynne, J. M. Lorio, and K. D. von Ellenrieder, "Visual-based navigation of an autonomous surface vehicle," *Mar. Technol. Soc. J.*, vol. 44, no. 2, pp. 37–45, 2010.



Patrick F. Rynne (S'09) received the Sc.B. degree in material engineering from Brown University, Providence, RI, in 2005 and the M.S. degree in ocean engineering from Florida Atlantic University, Boca Raton, in 2008. Currently, he is working towards the Ph.D. degree in applied marine physics at the University of Miami (UM), Miami, FL.

He has served as a Guest Investigator for the Deep Submergence Laboratory, Woods Hole Oceanographic Institute, Woods Hole, MA, in 2006 and 2008, and as a Research Assistant at the Florida Atlantic University SeaTech Center of Ocean Engineering Hydrodynamics Laboratory, Dania Beach, FL, from 2007 to 2010.

Mr. Rynne is currently a National Defense Science & Engineering (NDSEG) fellow at the UM Rosenstiel School of Marine and Atmospheric Science. He is a Member of the Marine Technology Society, IEEE Oceanic Engineering Society, and the American Society for Testing and Materials.



Karl D. von Ellenrieder (M'08) received the B.S. degree in aeronautics and astronautics from the Massachusetts Institute of Technology (MIT), Cambridge, in 1990 and the M.S. and Ph.D. degrees in aeronautics and astronautics from Stanford University, Stanford, CA, in 1992 and 1998, respectively.

Currently, he is an Associate Professor at the Department of Ocean Engineering, Florida Atlantic University, Dania Beach. Previously, he was a Postdoctoral Research Fellow at the Department of Mechanical Engineering, Monash University, Melbourne, Australia. His research interests include marine hydrodynamics, ship design, and the development of unmanned underwater and surface vehicles.

Prof. von Ellenrieder is a member of the Society of Naval Architects and Marine Engineers, the American Institute of Aeronautics and Astronautics, and the IEEE Oceanic Engineering Society.